Article

Not peer-reviewed version

Miocene Petit-Spot Basanitic Volcanoes on Cretaceous Alba Guyot (Magellan Seamount Trail, Pacific Ocean)

Igor S. Peretyazhko * , Elena A. Savina , Irina A. Pulyaeva

Posted Date: 19 August 2024

doi: 10.20944/preprints202408.1315.v1

Keywords: petit-spot volcanism; Miocene basanitic volcanoes; basanite; tuff; tuffite; lherzolite xenolith; Fe-Mn crust; biostratigraphy, calcareous nannofossils; Alba Guyot; Magellan Seamount Trail; Pacific Plate

Article

Miocene Petit-Spot Basanitic Volcanoes on Cretaceous Alba Guyot (Magellan Seamount Trail, Pacific Ocean)

Igor S. Peretyazhko [1,*], Elena A. Savina [1] and Irina A. Pulyaeva [2]

[1] Vinogradov Institute of Geochemistry, Russian Academy of Sciences, Siberian Branch, 664033 Irkutsk, Russia
[2] JSC Yuzhmorgeologiya, srtr. Krymskaya 20, Gelendzhik, 353461, Russia
* Correspondence: pgmigor@igc.irk.ru

Abstract: New data obtained from core samples of two boreholes in Alba Guyot in the Magellan Seamount Trail (MST), Western Pacific, including $^{40}Ar/^{39}Ar$ age of basanite, mineralogy of basanite, tuff, tuffite, mantle-derived inclusions in basanite and tuff (lherzolite xenolith and Ol, Cpx, Opx xenocrysts), and calcareous nannofossils biostratigraphy, have implications for the guyot history. Volcanics in the upper part of the Alba Guyot main edifice and its Oma Vlinder satellite, at sea depths between 3600 and 2200 m, were deposited during the Cretaceous 112 to 86 Ma interval. In the following ~60 myr, the Alba Guyot became partly submerged, and denuded with the formation of a flat summit platform while the respective fragment of the Pacific Plate was moving to the Northern Hemisphere. Volcanic activity in the northeastern part of the guyot summit platform rejuvenated in the Miocene (24–15 Ma) and produced onshore basanitic volcanoes and layers of tuff in subaerial and tuffite in shallow-water near-shore conditions. In Middle-Late Miocene (10–6 Ma), after the guyot had submerged, carbonates containing calcareous nannofossils were deposited on the porous surfaces of tuff and tuffite. Precipitation of the Fe-Mn crust (*Unit III*) recommenced during the Pliocene-Pleistocene (< 1.8 Ma) when the guyot summit reached favorable sea depths. The location of the MST guyots in the northwestern segment of the Pacific Plate near the Mariana Trench, along with the Miocene age and alkali-basaltic signatures of basanite, provide evidence for petit-spot volcanism on the Alba Guyot. This inference agrees with the geochemistry of Cenozoic petit-spot basaltic rocks from the Pacific and Miocene basanite on the Alba Guyot. The numerous volcanic cones reaching up to 750 m high and 5.1 km in base diameter, which were discovered on the Alba summit platform, provide the first evidence of voluminous Miocene petit-spot basanitic volcanism upon the Cretaceous guyots and seamounts of the Pacific.

Keywords: petit-spot volcanism; miocene basanitic volcanoes; basanite; tuff; tuffite; lherzolite xenolith; Fe-Mn crust; biostratigraphy; calcareous nannofossils; Alba Guyot; Magellan Seamount Trail; Pacific Plate

1. Introduction

Guyots in the Magellan Seamount Trail (MST) have been largely documented since the 1990s during cruise campaigns by the Research Department of the USSR/Russian Ministry of Geology, as well as by the Yuzhmorgeologia JSC and other institutions. The main results, including geological and geophysical maps, lithology, mineralogy, and chemistry of rocks, and data on Fe-Mn crusts, are available at http://guyot.ocean.ru, in technical reports of Yuzhmorgeologia, and in a number of publications [1–7], including our studies on the evolution of intraplate volcanism on guyots of Govorov and Alba [8–10].

Alba Guyot (17°00' N, 154°20' E) was named and renamed several times, and may be called in different ways in early and recent publications on the Pacific Plate volcanism. It was called

 doi:10.20944/preprints202408.1315.v1

Dalmorgeo, MAGL-3 or MA-15 in the Russian-language literature, while publications in English used the names Vlinder for the main edifice and Oma Vlinder for its SE satellite [4,5,7]. In 2004, the GEBCO Subcommittee of Undersea Feature Names approved a new name of Alba after Francisco Alba, a companion of Ferdinand Magellan.

The guyot has a shape of a truncated square prism with a 126×90 km pedestal at a bathymetric level of 5100 m and comprises a main edifice surrounded by several satellites (Figure 1a). The slopes of the main edifice dip at 35–40° near the top and flat out to 2–8° at the base. The 46×35 km flat top is at sea depths of 1250–1500 m. As evidenced by geophysical surveys, photo and video-profiling, dredging, and shallow drilling (within 1–1.5 m), the guyot is mainly composed of volcanic rocks, with subalkaline and alkali basalt varieties exposed on the slopes between the 3000 m sea depth and the summit [2]. The sediments deposited on the submerged guyot consist of shallow-water and hemipelagic limestone, carbonate-cemented breccia, carbonate, and mudrock lithologies. The cover of the summit platform consists partly of foraminifera silt and an up to 15 cm thick Fe-Mn crust on surfaces free from sediments, mainly along the guyot edge.

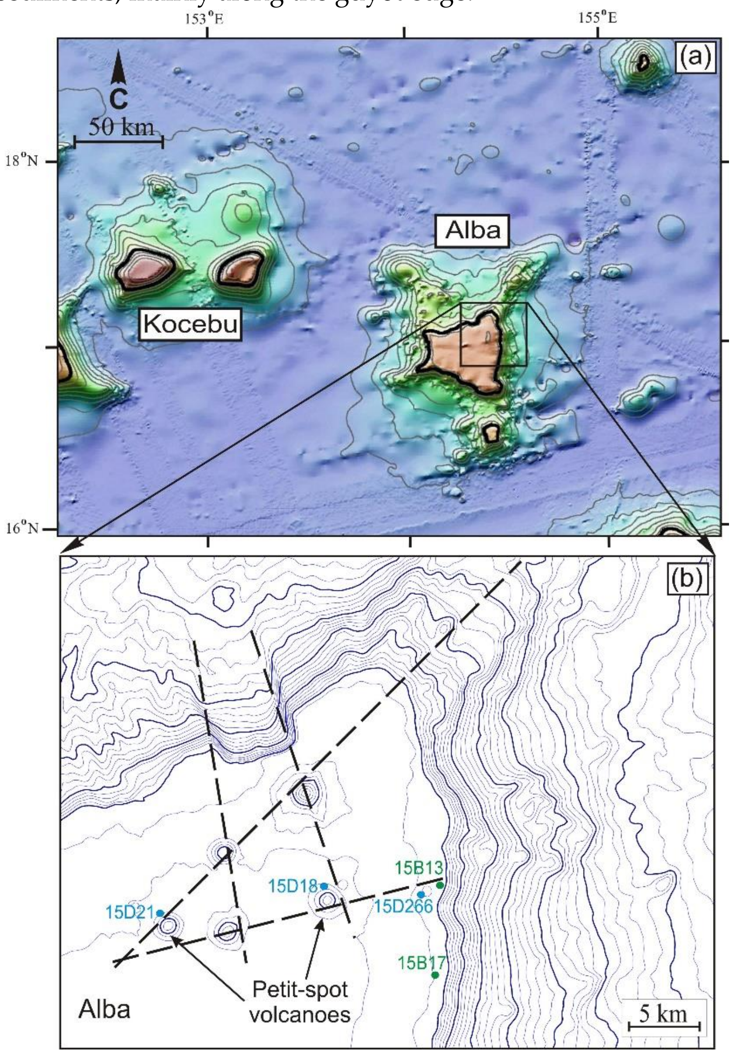

Figure 1. Bathymetry map of Kocebu and Alba Guyots (a); enlarged fragments of the main Alba Guyot edifice (b), modified from Peretyazhko et al. [9]. Panel (b) shows inferred faults and cones of petit-spot volcanoes. Location of sampling sites (Table 1): 15D21, 15D18, and 15D266 dredges; 15B13 and 15B17 boreholes. Bold lines in panels (b) are isobaths at 100 m intervals.

Fe-Mn crusts precipitated from seawater make up condensed stratigraphic sequences which record the accumulation of metals, as well as the Cenozoic evolution of the oceanic environment in general. Deposition of Fe and Mn oxyhydrates in the MST area lasted 60–65 myr in total and was interrupted by episodes of partial dissolution. The discontinuous precipitation process produced five

Preprints.org (www.preprints.org) | NOT PEER-REVIEWED | Posted: 19 August 2024 doi:10.20944/preprints202408.1315.v1

units of Fe-Mn crusts that differ in structure, texture, composition, and age [11–13]: Late Paleocene-Early Eocene (*Unit I-1*), Middle-Late Eocene (*Unit I-2a*), Late Oligocene-Early Miocene (*Unit I-2b*), Middle-Late Miocene (*Unit II*), and Pliocene-Pleistocene (*Unit III*). The most complete sections resulting from successive deposition of Fe-Mn layers *I-1* → *I-2a* → *I-2b* → *II* → *III* display three gaps of Early-Middle Oligocene (~12 myr), Early Miocene (~ 4 myr), and Early Pliocene (~ 1.6 myr). The longest gap separates the Paleocene-Eocene and Miocene-Pleistocene events, which correspond to older (*I-1, I-2a*) and younger (*II, III*) units. Fe-Mn crust samples often represent reduced sections that record local mineralization conditions in different zones of guyot and seamount surfaces. The gap between older and younger units may exceed 20 myr. Most of Fe-Mn crusts display the *I-1* → *I-2a* → *II* → *III* and *I-1* → *II* → *III* successions.

We report new data on Cenozoic volcanics that build several cones on the flat summit platform of Alba Guyot revealed by bathymetric survey in its northeastern part (Figure 1). The scope of work in cruises of 2019–2020 on R/V Gelendzhik included dredging at a small cone (15D266 dredge) and drilling of volcaniclastic rocks and a Fe-Mn crust (15B13 and 15B17 boreholes) in the guyot's northeastern edge (Table 1). The samples of basanite, a lherzolite xenolith from basanite, tuff, and tuffite were analysed, including $^{40}Ar/^{39}Ar$ age of basanite, mineralogy of basanite, tuff, mantle-derived inclusions (lherzolite xenolith and Ol, Cpx, Opx xenocrysts), and calcareous nannofossils biostratigraphy found in the 15B13 and 15B17 cores. The earlier [9] and new data provide evidence of voluminous Miocene eruptions of basanitic magma on the guyot. The results have geodynamic implications and allow new insights into the Miocene petit-spot basanitic volcanism on Alba Guyot, as well as a more general idea of Cenozoic intraplate alkali-basaltic petit-spot volcanism in the subducting northwestern Pacific Plate.

Table 1. Location of sampling sites at Alba Guyot.

Sample	Type sampling	Latitude (°N)	Longitude (°E)	Sea depth, m
15D266	Dredging	17.019914	154.426390	1414
15D21	Dredging	17.0104830	154.2580171	1202
15D18	Dredging	17.0256170	154.3648169	922
15B13	Drilling	17.0281988	154.4403234	1148
15B17	Drilling	16.9563422	145.4331726	1409

Dredging was performed within a 600 m long interval; coordinates are for the starting point.

2. Materials and Methods

The samples collected from Alba Guyot were analyzed at several institutions. Most of the analyses were performed at the Center for Isotope-Geochemical Studies of the Vinogradov Institute of Geochemistry, Siberian Branch of the Russian Academy of Sciences (IGC, Irkutsk).

2.1. XRF and SEM-EDS

Samples of volcanic rocks were analyzed for bulk chemistry by on a Bruker AXS S4 Pioneer wavelength dispersive X-ray fluorescence spectrometer using glass fusion discs (major oxides), as well as methods of titration (FeO, CO_2), and gravimetric analysis (H_2O^+, H_2O^-, and total sulfur). The mineral and phase compositions were studied by scanning electron microscopy coupled with energy-dispersive spectrometry (SEM EDS) on a Carl Zeiss LEO-1430VP electron microscope equipped with an INCA Energy 350 analytical system at the Geological Institute (GI, Ulan-Ude), and on a Tescan Mira-3 LMU high-resolution electron microscope with an Ultim MAX-40 SDD detector at IGC (Irkutsk). The analyses were run in a scanning mode on carbon-coated polished cut surfaces of samples, at 1–10 μm² spots, 20 kV accelerating voltage, 1 nA beam current, and 30 s acquisition time (excluding dead time). The data quality was checked against analyses of reference samples, including quartz, albite, orthoclase, wollastonite, MgO, Al_2O_3, CaF_2, metals, and synthetic compounds from sets 6316 and 7682 of the reference standards by Microanalysis Consultants Limited (Oxford Instruments Ltd., UK). All the calculations and matrix corrections were done automatically with INCA and AZtec

Preprints.org (www.preprints.org) | NOT PEER-REVIEWED | Posted: 19 August 2024 doi:10.20944/preprints202408.1315.v1

software (Oxford Instruments Nanoanalysis, UK). Silicate glasses were scanned over >10 μm² spots, which allowed reducing the loss of alkalis and effects of the microtopography of polished samples on data quality. The detection limits of major elements were 0.2–0.3 wt%. Average random errors for major elements varied depending on their contents: ± 0.9 rel% at > 10 wt%, ± 3.0 rel% at 1–10 wt%, and ± 13 rel% at 0.3–1 wt% [14].

Mineral formulas and mass-balance calculations were performed in Crystal software, ver. 3.0 [15].

2.2.40. Ar/^{39}Ar Dating

Basanite sample 15D266A selected for dating was crushed to 250–500 μm and freed from coarse clasts of authigenic calcite, altered material, and Fe-Mn crust fragments under a binocular. The cleaned sample were crushed further, sieved to 150–250 μm, and leached in a 4N HNO_3 solution for 10 min at room temperature in order to remove remnant calcite, volcanic glass, and soluble products of seawater alteration. Finally, the crushed material was rinsed several times with ultrapure water, till neutral pH of the solution. Incremental heating $^{40}Ar/^{39}Ar$ dating was applied to two specimens of the same crushed rock fraction digested in 4N HNO_3. The specimens were wrapped in aluminum foil together with the BERN-4M muscovite standard certified as a $^{40}Ar/^{39}Ar$ reference (18.7 ± 0.096 Ma) and placed in a quartz capsule which was vacuumed and welded shut. The samples were irradiated in the cadmium-plated channel of the VVR-K research reactor at the Tomsk Polytechnical University, Tomsk, Russia. The stepwise heating experiments from 500 °C to 1150 °C were run in a quartz reactor with an external heating element. A blank run for ^{40}Ar determination (10 min at 1200 °C) did not exceed 5×10−10 ncm³. Argon for the measurements was cleaned using ZrAl–SAES getters. The Ar isotope ratios were determined on a Noble Gas 5400 (MicroMass, UK) and on a Thermo Scientific Argus VI mass spectrometer at the Analytical Center for Multielemental and Isotopic Studies of the V.S. Sobolev Institute of Geology and Mineralogy (IGM, Novosibirsk). The $^{40}Ar/^{39}Ar$ ages were calculated for each temperature step of incremental heating and plateau ages were obtained according to cumulative ^{39}Ar released.

2.3.C. alcareous Nannofossils Biostratigraphy

Mocro-nannofossils were detected and identified in chips of core fragments, under a Jeol JSM 6390LA scanning electron microscope, at the Botanical Institute (St. Petersburg). The rock chips, ≤ 5 mm in size, were mounted on a metal holder, spur coated with gold (60–90 Å), and examined at magnifications up to ×20000 with an accelerating voltage of 18 kV. The BSE images were used for taxonomic classification of the fossils, at the genus or species level. The age of the respective core intervals was determined according to nannoplankton species, with a focus on index species of main biozones and subzones [16–18]. The intervals of the identified calcareous nannofossils were correlated with ample biostratigraphic evidence from oceanic sediments [16–24].

3. Results

The basaltic rocks of submerged Alba Guyot have been weathered more or less strongly under the effect of sea water, whereby an iddingsite aggregate (mixture of montmorillonite, chlorite, goethite, and other phases) replaced olivine (Ol) while a fine aggregate of palagonite (hydrated quenched glass) and secondary minerals partially replacing of the vitreous matrix. Vugs and cracks in volcanic rocks are often filled with authigenic calcite and organic-bearing phosphate-carbonate material; locally phillipsite, chlorite, and other secondary phases precipitated in vugs.

3.1. Core Samples

Borehole 15B13 drilled at the base of a cone near dredging site 15D266 (Figure 1b) stripped a Fe-Mn crust (*Unit III*), up to 3 cm thick (2.8 cm on average) lying over brick-red porous tuff (Figure 2). The core interval between 2.8 and 16 cm contains angular tuff clasts, from few mm to 3 cm long, amidst biomorphic carbonate cement and alteration products of fine glass and volcanic material. The tuff in the 16–42 cm interval is more porous and almost lacks carbonate inclusions.

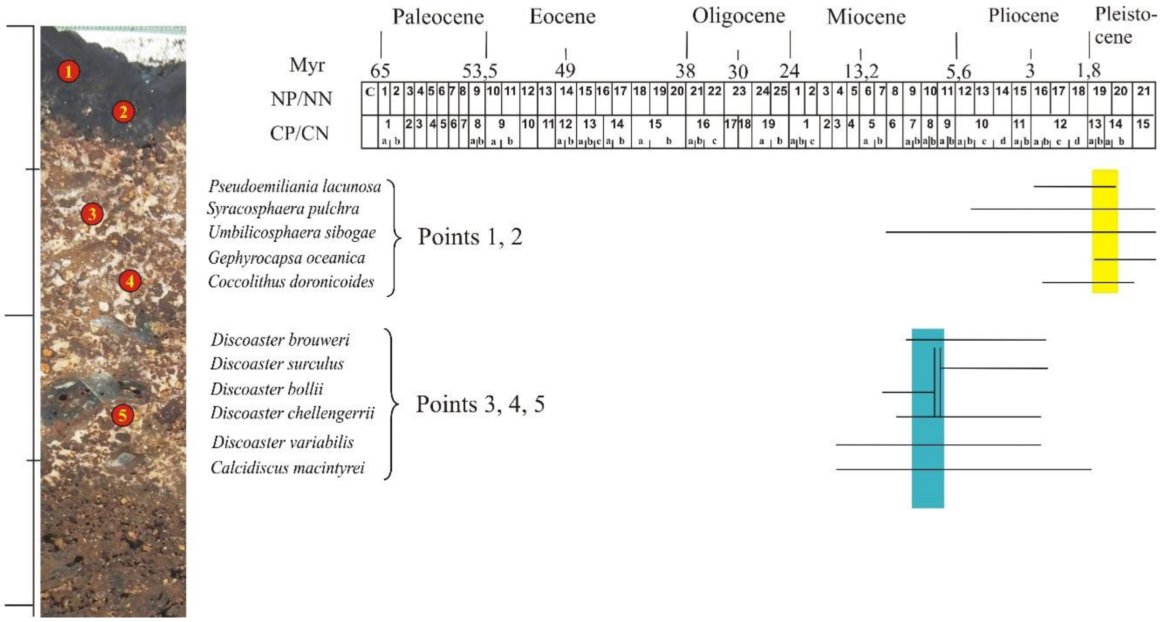

Figure 2. Calcareous nannofossil biostratigraphy, core sample 15B13. Nannofossils were found and identified in Fe-Mn crust (*Unit III*, points 1 and 2) and in tuff section at points 3, 4, and 5. Colored zones show age ranges for different samples based on extant periods for identified nannoplankton species. Cenozoic time scale is based on Neogene (NN), Martini [16], (CN), Okada, Bukry [22], and Palaeogene (NP), Martini [16], and (CP) Okada, Bukry [22] zonal scales correlated to ages by Shumenko [24]. Numbers 1 to 21 refer to zone numbers.

Borehole 15B17 drilled at the eastern edge of the guyot (Figure 1b) stripped several units of the Fe-Mn crust and tuffaceous material (Figure 3). *Unit III* of the Fe-Mn crust, with sporadic carbonate inclusions, occupies the top 1.2 cm of the core above volcaniclastic tuffite with planktonic limestone, sand-size clasts of palagonite, and few fine detrital Cpx and Ol grains in a silt-pelitic groundmass (1.2–4 cm). The 4–8.5 cm interval encompasses *Unit I-2b* of the Fe-Mn crust containing two concretions in a carbonate-phosphate matrix partly damaged during drilling. The concretions enclose basaltic clasts in the central part. The lower portion of the core (8.5–14 cm) is composed of *Unit I-1* of the Fe-Mn crust and basaltic clasts.

Preprints.org (www.preprints.org) | NOT PEER-REVIEWED | Posted: 19 August 2024 doi:10.20944/preprints202408.1315.v1

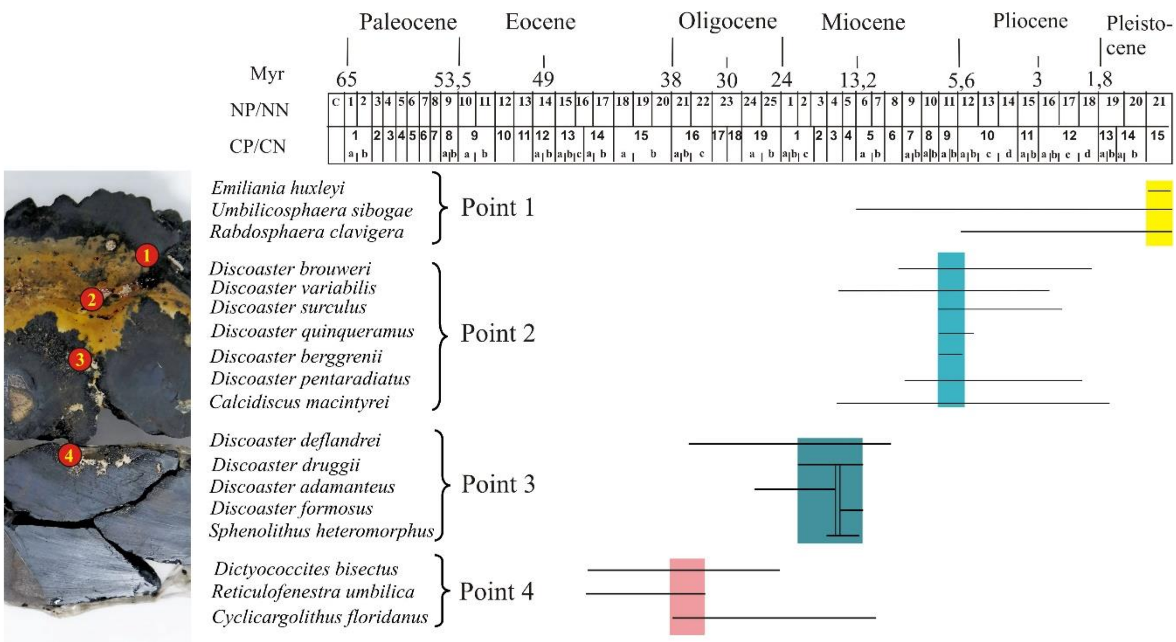

Figure 3. Calcareous nannofossil biostratigraphy of core sample 15B17. Nannofossils were identified and their respective extant periods were determined for Fe-Mn crust (*Unit III*, point 1); tuffite; point 2; carbonate inclusions in buried nodules, *Unit I-2b*, point 3; carbonate inclusions at the contact between *Units I-1* and *I-2b*, point 4. Colored zones show age ranges for different samples. Cenozoic time scale is based on zonal scales (see Figure 2 for explanations).

3.1.1. Calcareous Nannofossil Biostratigraphy

The 15B13 and 15B17 core samples of rocks and Fe-Mn crust material contain calcareous planktonic nannofossils of golden-brown coccolithophores and discoasters. They are commonly better preserved than other calcareous microfossils (e.g., formainifera) and can be identified from prints even when completely dissolved.

We analyzed two Fe-Mn crust chips and three samples of carbonate inclusions in tuff from the upper 16 cm of the 15B13 core (Figure 2). BSE images of the Fe-Mn crust (*Unit III*, points 1 and 2) reveal well pronounced casts of coccolithophores healed with by iron and manganese oxyhydrates. The samples from this interval contain a nannoplankton assemblage composed of *Pseudoemiliania lacunosa*, *Syracosphaera pulchra*, *Umbilicosphera sibogae. Gephyrocapsa sp. cf. G. oceanica*, and *Coccolithus sp. cf. C. doronicoides* (Figure 4). The identified species coexisted during biozones CP13 – CP14a. Abundant *Pseudoemiliania lacunosa*, an index species of zone NN19, marks an Early Pleistocene age of the Fe-Mn crust (*Unit III*).

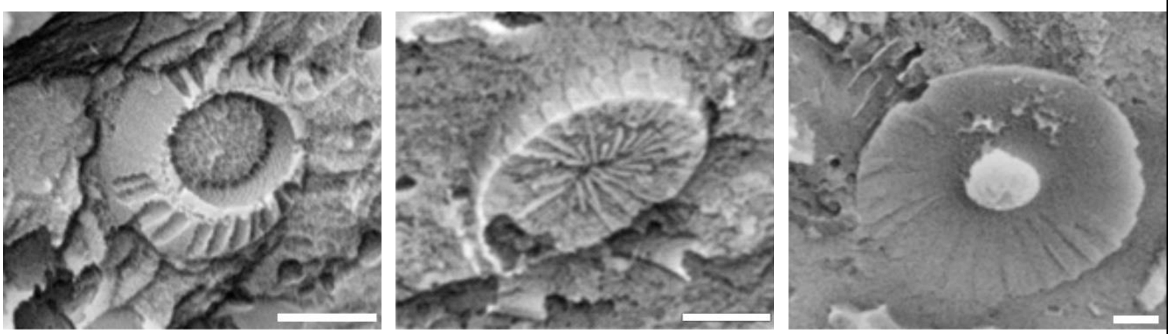

Pseudoemiliania lacunosa (Kamptner) Gartner (CN11b – CN14a)	*Syracosphaera pulchra* Lohmann (CN10 – CN15)	aff. *Umbilicosphaera sibogae* Gaarder (CN5 – CN15)

doi:10.20944/preprints202408.1315.v1

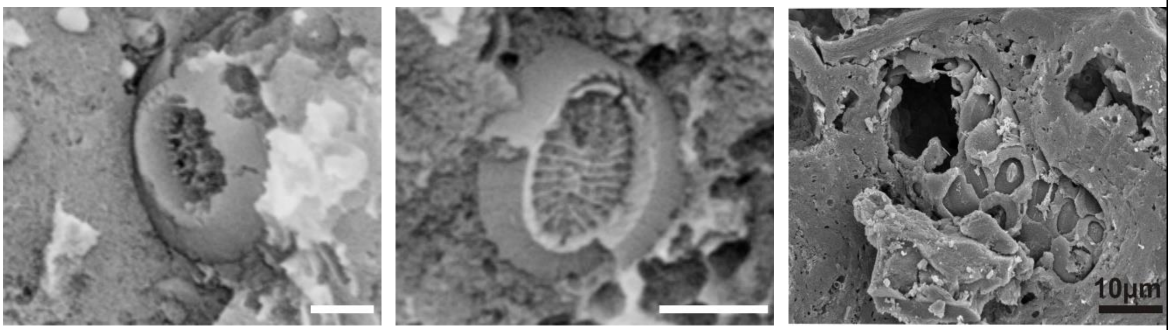

Gephyrocapsa sp. cf. *G. oceanica* (Kamptner) (CN14a – CN15) | *Coccolithus* sp. cf. *C. doronicoides* (CN12 – CN14) | Taxonomically uncertain nannoplankton fossils

Figure 4. Early Pleistocene calcareous nannofossils (biozones NN19, CP13 – CP14a) in *Unit III* of Fe-Mn crust, (core 15B13, interval 0–2.8 cm, points 1 and 2). Scale bar 1 μm, if not indicated in BSE images.

Samples of carbonate cement from tuff, core depths 2.8 to 16 cm (points 3, 4, 5 in Figure 2), contain Miocene-Pliocene planktonic species of *Discoasteraceae*: most frequent *Discoaster brouweri* and *D. Surculus* (Figure 5), rarer *Discoaster variabilis*, *Discoaster* cf. *D. chellengerrii* and *Discoaster bollii*, and sporadic *Calcidiscus macintyrei* and *Scyphosphaera* sp. cf. *S. aranta*. All these species were extant during Middle-Late Miocene biozones CN7 and CN8.

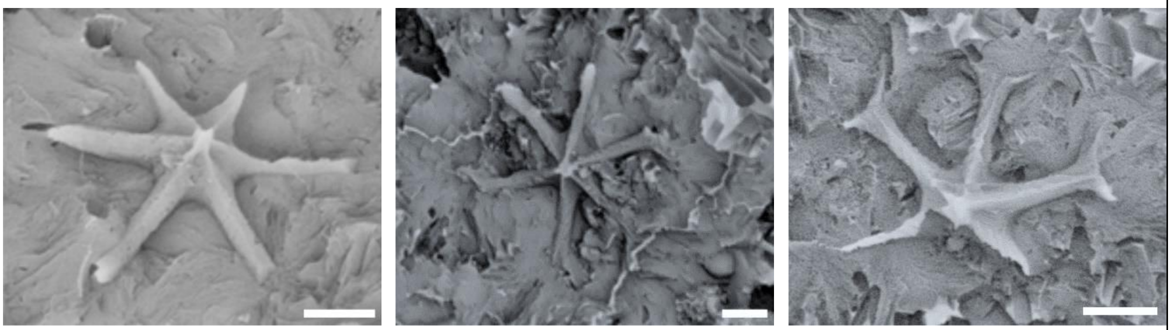

Discoaster brouweri Tan (CN7a – CN12d) | *Discoaster surculus* Martini & Bramlette (CN9a – CN12b)

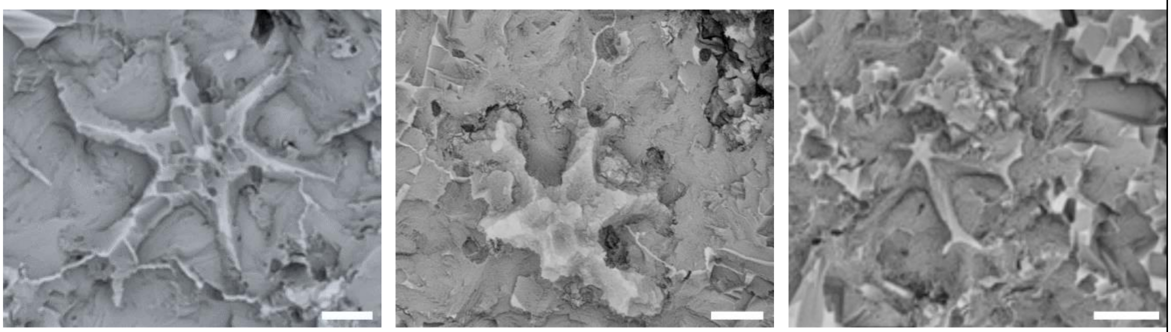

Discoaster cf. *D. chellengerrii* Bramlette & Riedel (CN6 – CN12a) | *Discoaster variabilis* Martini & Bramlette (CN3 – CN12a) | *Discoaster bollii* Martini & Bramlette (CN5b – CN8a

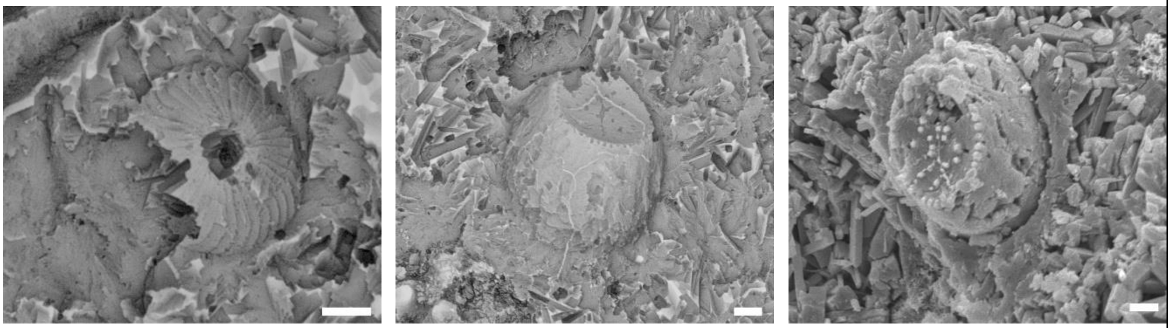

Calcidiscus macintyrei Loeblich & Tappan (CN3 – CN12a) | *Scyphosphaera* sp. cf. *S. aranta* | *Scyphosphaera* sp.

Figure 5. Middle-Late Miocene calcareous nannofossils from carbonate cement in tuff (core 15B13, interval 2.8–16 cm, points 3, 4, 5). Scale bar 2 μm.

The biostratigraphy of core 15B17 was studied in four Fe-Mn crust and tuffite samples (Figure 3). Prints of calcareous nannofossils were found in a homogeneous matrix of the Fe-Mn crust (*Unit III*), and original fossil remains also occurred in clay-carbonate inclusions (point 1). The nannoplankton assemblage includes Pliocene-Pleistocene species of *Umbilicosphaera sibogae*, *Rhabdoshaera clavigera*, *Emiliania huxleyi*, *Ceratolithus cristatus*, *Coccolithus pelagicus*, *Helicosphaera carteri*, and *Cyclococcolithina leptopora* (Figure 6). Taking into account the presence of the *Emiliania huxleyi* index species, the taxa identified at point 1 were extant during biozone CN15 (Late Pleistocene).

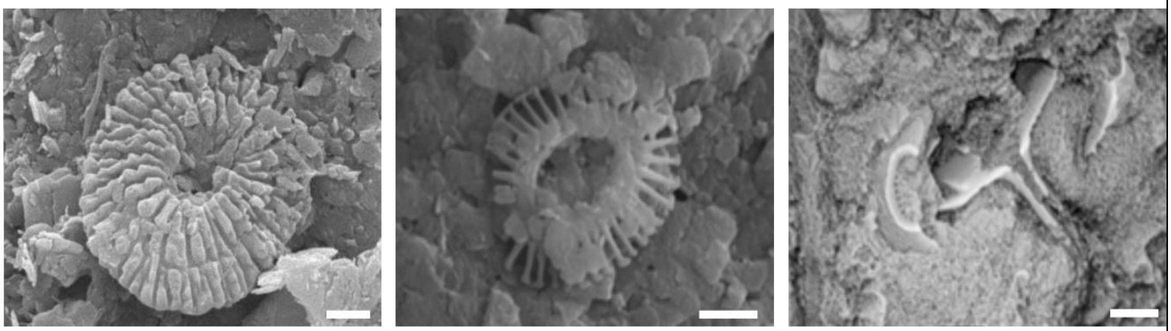

Umbilicosphaera sibogae Gaarder (CN5-CN15) | *Emiliania huxleyi* (Lohmann) Hay & Mohler (CN15) | aff. *Rabdosphaera clavigera* Murray (CN10 – CN15)

Figure 6. Pleistocene calcareous nannofossils from Fe-Mn crust, *Unit III* (core 15B17, interval 0–1.2 cm, point 1). Scale bar 1 μm.

Carbonate inclusions in the tuffite layer bear abundant discasters and coccolithophores. The nannoplankton assemblage is mainly composed of *Discoasteraceae* (Figure 3, point 2): most frequent *Discoaster brouweri*, *D. variabilis*, and *D. surculus*, which were extant from the Late Miocene through the Pliocene (biozones CN9 – CN12a) (Figure 7); rare *Cyclococcolithus leptoporus* and *Scyphoshaera globulata*; sporadic Late Miocene index species of *D. berggrenii*, *D. pentaradiatus* and *D. quinqueramus* (lower and upper boundaries of biozone CN9).

Preprints.org (www.preprints.org) | NOT PEER-REVIEWED | Posted: 19 August 2024 doi:10.20944/preprints202408.1315.v1

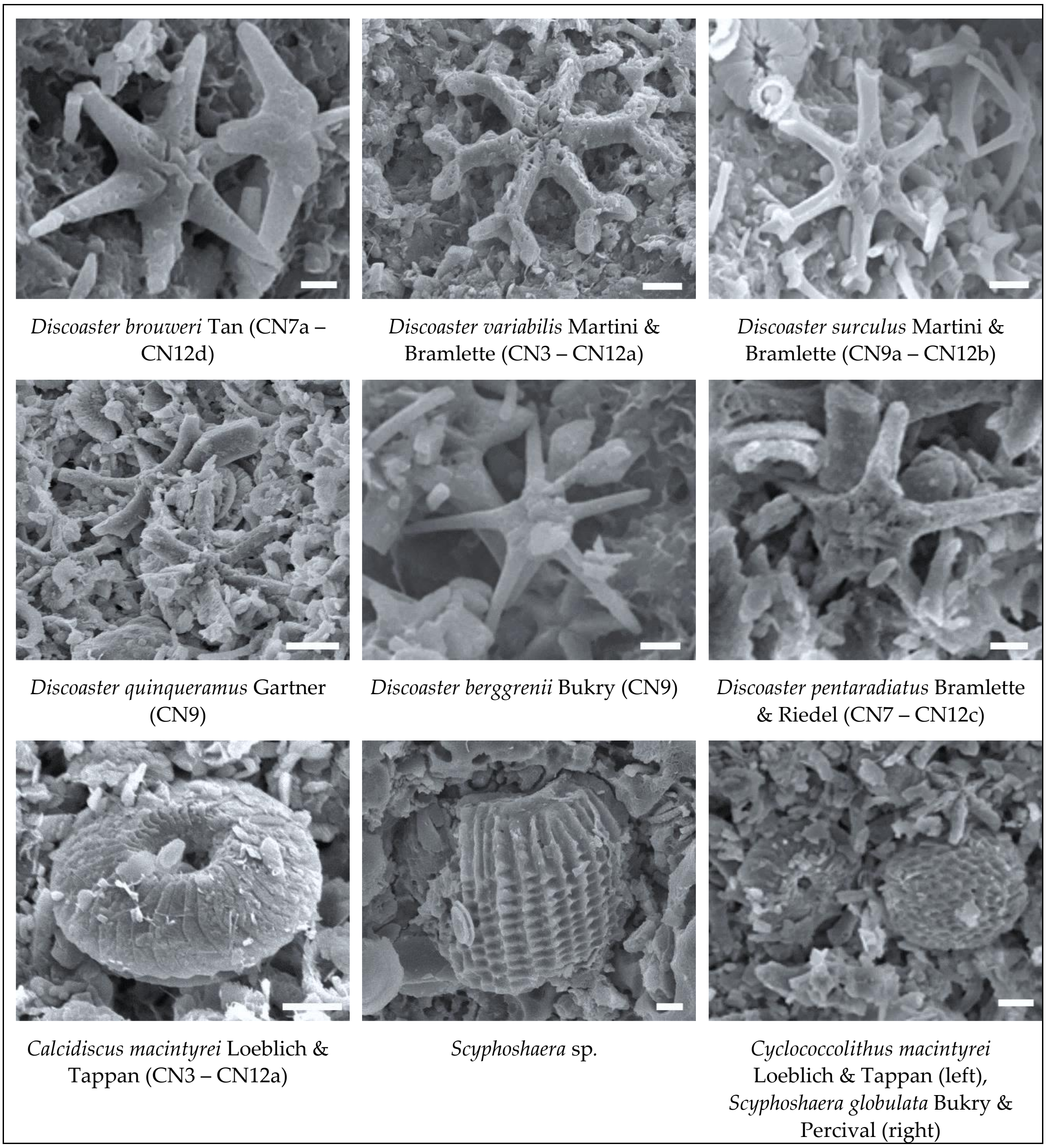

Figure 7. Late Miocene calcareous nannofossils from tuffite (core 15B17, interval 1.2–4 cm, point 2). Scale bar 2 μm.

Calcareous nannofossils were also found in a carbonate inclusion at larger core depths, between two buried Fe-Mn crust units (Figure 3, point 3). The assemblage comprises most abundant Discoasteraceae species of *Discoaster deflandrei*, *Discoaster druggii*, and *Discoaster adamanteus*, less frequent *Discoaster formosus*, as well as *Sphenolithus genus* (*Sphenolithaceae*) morphologically similar to *Sphenolithus heteromorphus* (Figure 8), which were extant during Early Miocene biozones CN1 – CN4.

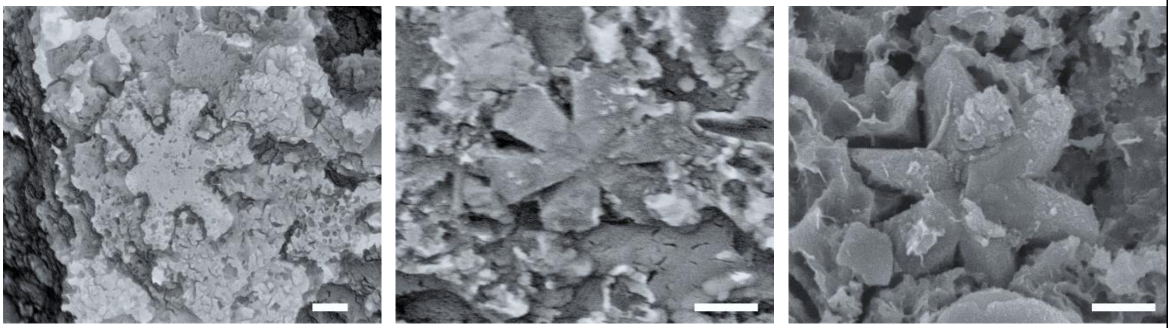

Discoaster deflandrei Bramlette & Riedel (CP16c – CN5b)

Discoaster druggii Bramlette & Wilcoxon (CN1c – CN4)

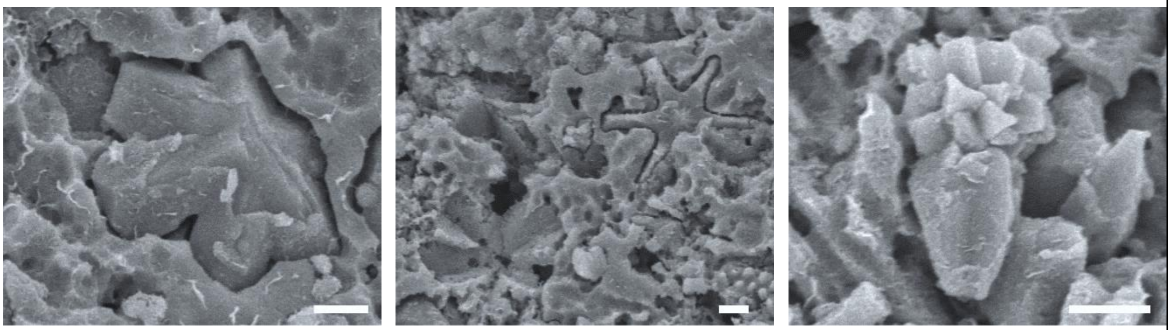

Discoaster adamanteus Bramlette & Wilcoxon (NP19a – CN2)

Discoaster adamanteus Bramlette & Wilcoxon (left), *Discoaster formosus* Martini & Worsley (CN4)

Sphenolithus heteromorhus Deflandre (CN3 – 4)

Figure 8. Late Oligocene-Early Miocene calcareous nannofossils from limestone between Fe-Mn crust units (core 15B17, interval 4.0–8.5 cm, point 3). Scale bar 2 µm.

Carbonate inclusions at the contact of *Unit I-1* of the Fe-Mn crust with the overlying layer in the lower portion of the core (Figure 3, point 4) bear quite well preserved coccolithophores. The identified species are: *Dictyococcites bisectus* (Hay, Mohler, & Wade) Bukry & Percival, *Reticulofenestra umbilica* Martini, *Coccolithus pelagicus* Bukry, and *Cyclicargolithus floridanus* Bukry (Figure 9). This assemblage is typical of biozones CP14 – CP16 that span the Late Eocene – Early Oligocene period, while the identified species coexisted within biozone CP16.

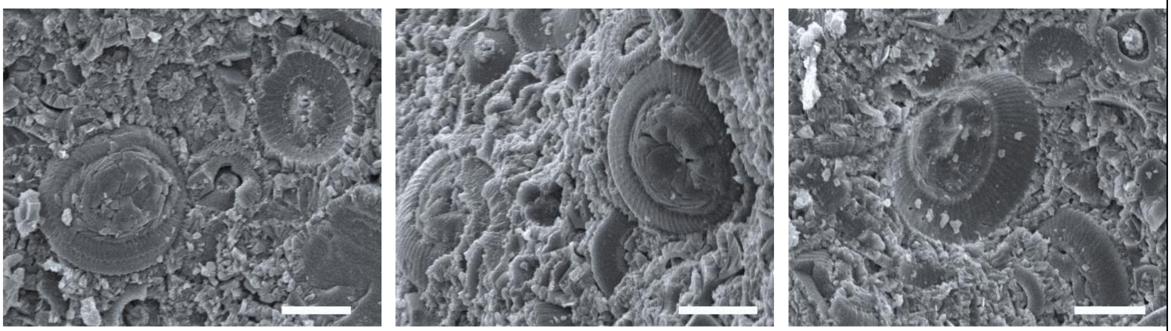

Dictyococcites bisectus (Hay, Mohler, & Wade) Bukry & Percival (CP14a – CP19b)

Reticulofenestra umbilica Martini (CP14a – CP16c)

Preprints.org (www.preprints.org) | NOT PEER-REVIEWED | Posted: 19 August 2024 doi:10.20944/preprints202408.1315.v1

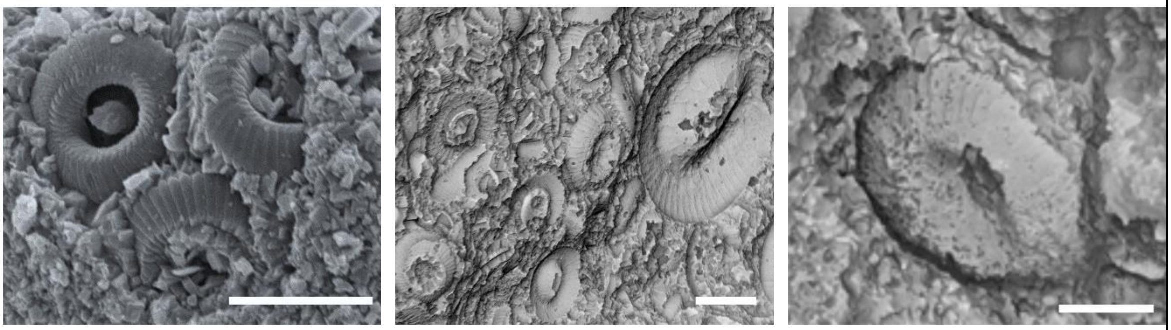

Cyclicargolithus floridanus Bukry (CP16a – CN5a)

Coccolithus pelagicus Bukry (transient species)

Figure 9. Late Eocene-Early Oligocene calcareous nannofossils from limestone above *Unit I-1* of the Fe-Mn crust, (core 15B17, interval 8.5–14.0 cm, point 4). Scale bar 5 µm.

3.2. Volcanic and Mantle Rocks

Basanite sample 15D266A has a porphyritic texture, with phenocrysts of olivine (Ol) and clinopyroxene (Cpx), without plagioclase, in a vuggy aphyric matrix. Olivine phenocrysts contain melt inclusions and spinel (Sp) grains. The hyalopelitic matrix is composed of randomly oriented euhedral Cpx and Ol microlites, titanomagnetite (Ti-Mgt) dendritic crystals and grains, and rare Sp grains rimmed with Ti-Mgt (Figure 10a), with interstitial glass, as well as frequent small and large Ol, orthopyroxene (Opx), and Cpx xenocrysts. Coarse (0.5–3 mm) angular Ol, Cpx and Opx xenocrysts are rimmed with newly formed Ol, Cpx or Cpx + Ol aggregate, respectively (Figure 10b,c). The matrix and the glass are partly weathered by sea water. The major-element chemistry of basanite and average oxide contents in minerals and glass are presented in Table 2.

Basanite from site 15D266B encloses a xenolith of lherzolite (10×12 cm in the largest section) with a coarse protogranular texture and a massive structure (Figure 10d). Its yellowish-brownish color is due to a large percentage of iddingsite aggregate partly replacing Ol. The amount of iddingsite reaches 33.4 wt%, as estimated by mass balance calculations [9], and the modal composition of lherzolite reconstructed with regard to average mineral chemistry of the constituent phases is 57.3 wt% Ol, 26 wt% Opx, 14 wt% Cpx, and 2.7 wt% Sp. Large particles of spinel in lherzolite are intergrown with Cpx, Opx, and Ol (Figure 10e,f). Cpx encloses quasi-parallel aligned exsolution lamelli of Opx and Sp, as well as round inclusions of pyrrhotite, while Opx encloses sporadic Cpx lamelli (Figure 10f). The original and reconstructed bulk compositions of lherzolite and average oxide contents in mantle minerals are presented in Table 3.

Preprints.org (www.preprints.org) | NOT PEER-REVIEWED | Posted: 19 August 2024 doi:10.20944/preprints202408.1315.v1

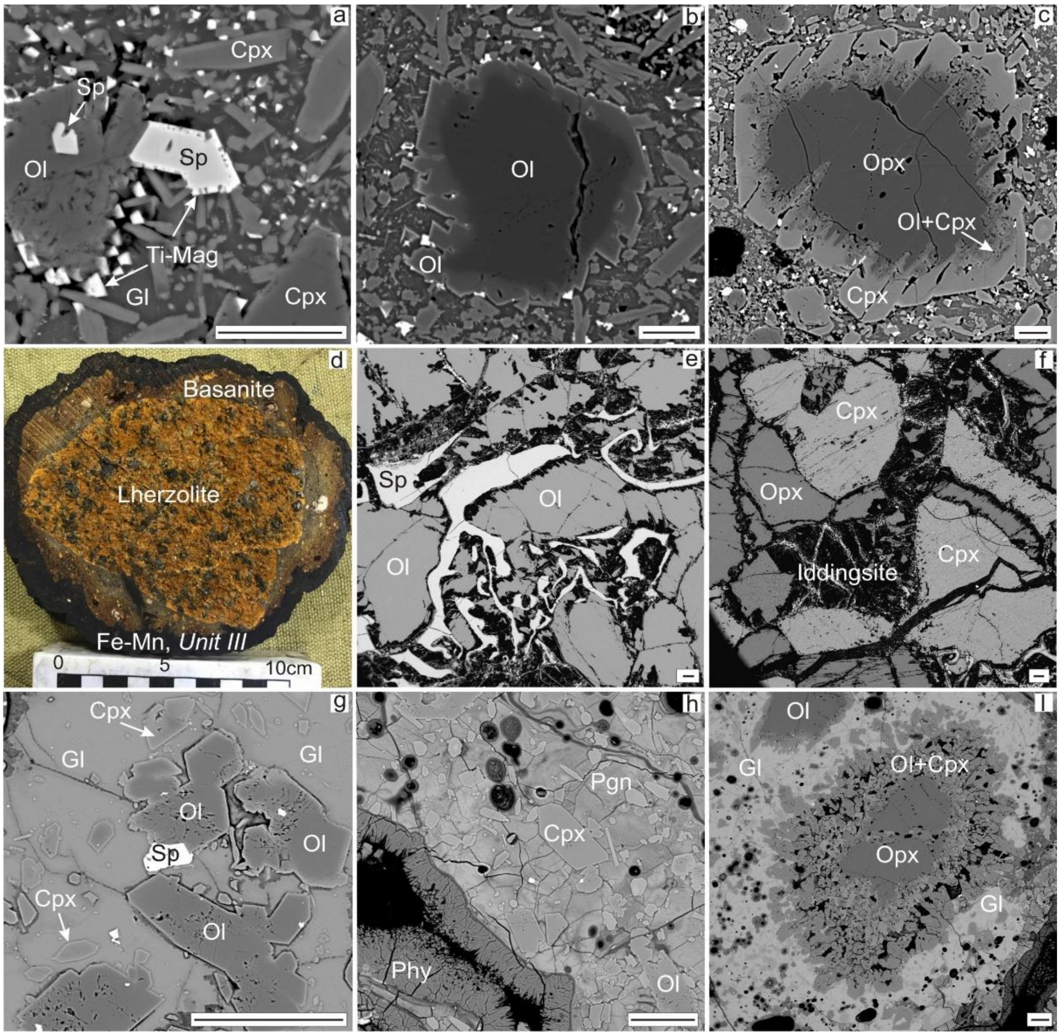

Figure 10. Matrix fragments of basanite 15D266A (a–c), lherzolite xenolith 15D266B (d–f), and tuff 15B13 (g–i). Abbreviations stand for Ol = olivine, Opx = orthopyroxene, Cpx = clinopyroxene, Sp = spinel, Ti–Mag = Ti-magnetite, Gl = glass, Fe-Mn = ore crust, Pgn = palagonite, Phy = phyllipsite. Scale bar 20 μm for (a,b,c), and 100 μm for (e,f,g,h,l).

Table 3. Major-element chemistry of lherzolite xenolith and its constituent minerals (wt%).

	15D266B		**Ol**	**Opx**	**Cpx**	**Sp**
	1	2	3(37)	4(26)	5(38)	6(51)
SiO_2	42.29	45.26	40.24	55.63	52.67	
TiO_2	0.11	0.06			0.22	
Al_2O_3	3.85	2.52		3.02	3.30	47.13
FeO	5.11	7.53*	9.09	5.73	1.15	11.28
Fe_2O_3	8.80			0.53	0.95	2.88
MnO	0.23	0.12	0.10	0.12		
MgO	33.15	40.02	49.31	33.53	16.13	18.08
CaO	3.78	3.38		0.38	23.16	
Na_2O	0.59	0.12			0.76	
K_2O	0.15					
P_2O_5	0.21					
NiO		0.26	0.42			0.21
Cr_2O_3		0.74		0.39	0.76	18.79
V_2O_3						0.09
ZnO						0.25

Preprints.org (www.preprints.org) | NOT PEER-REVIEWED | Posted: 19 August 2024 doi:10.20944/preprints202408.1315.v1

H_2O-	0.46					
H_2O+	0.96					
Total	99.94	100.00	99.16	99.34	99.12	99.61
			Fo 90.6	Mg# 90.5	Mg# 93.5	Cr# 0.22

Sample 15D266B also contains 0.22 wt% CO_2, and 0.03 wt% S tot. Major-element composition of lherzolite (column 2) was calculated from average analyses of Ol, Cpx, Opx, and Sp corrected for Ol replaced by iddingsite aggregate [9]. * All iron as FeO. The contents of FeO and Fe_2O_3 in minerals are calculated by stoichiometry. Fo, 100·Mg/(Mg+Fe); Mg#, 100·Mg/(Mg+Fe); Cr#, Cr/(Cr+Al).

Tuff from core 15B13 (Figure 2) is composed of unsorted volcanic glass clasts with inclusions of euhedral phenocrysts and microlites of Cpx, Ol, and rare Sp grains. The tuff clasts contain small peridotite xenoliths, as well as Ol, Cpx, and Opx xenocrysts. The bulk composition of tuff and average oxide contents in minerals are presented in Table 4. The predominant volcanic rock in tuff is similar to 15D266A basanite in its mineral assemblage (see below), while the small peridotite xenoliths and xenocrysts of Ol, Cpx and Opx are compositionally similar to 15D266B lherzolite.

Table 4. Composition of tuff, its constituent minerals and glass (wt%).

	15B13	**Ol**		**Cpx**	**Opx**	**Sp**	**Glass**
	1	2(39)	3(46)	4(59)	5(84)	6(30)	7(121)
SiO_2	44.28	39.48	40.62	50.38	55.14	0.60	46.34
TiO_2	2.39			1.38		2.65	3.10
Al_2O_3	10.36			2.97	2.39	14.81	14.52
FeO		14.39	9.34	3.90	5.73	21.43	10.47**
Fe_2O_3	12.84*			2.28	0.17	12.58	
MnO	0.18	0.22	0.14	0.08	0.15		0.16
MgO	11.94	44.73	49.09	15.27	33.33	9.72	4.14
CaO	4.42	0.29	0.12	22.01	0.38	0.28	8.42
Na_2O	2.81			0.44			4.06
K_2O	2.54						3.58
P_2O_5	0.32						1.27
LOI	8.79						
NiO		0.31	0.40			0.14	
Cr_2O_3				0.54		35.73	
V_2O_3						0.16	
Total	100.95	99.42	99.71	99.26	97.63	98.10	96.42
		Fo 84.9	Fo 90.4	Mg# 81.9	Mg# 91.0	Cr# 0.62	

Glass also contains 0.18 wt% BaO, 0.11 wt% SO_3, and 0.18 wt% Cl. * All iron as Fe_2O_3. ** All iron as FeO. The contents of FeO and Fe_2O_3 in minerals are calculated by stoichiometry. LOI = loss on ignition.

3.2.1. Chemistry of Minerals and Glasses

Olivine in volcanics becomes easily replaced by an iddingsite aggregate under a prolonged effect of sea water but is present in abundance in the lherzolite xenolith, basanite, and tuff (Table 2–4). Olivine phenocrysts and microlites in tuff and basanite contain similar amounts of the Fo component (100·Mg/(Mg+Fe) 82.2–86.5 mol%) and NiO (0.15–0.42 wt%). Olivine in lherzolite, peridotite xenoliths, and xenocrysts from basanite and tuff has the highest Fo of 89.5–91.7 mol% and is richer in NiO 0.31–0.57 wt% (Figure 11a).

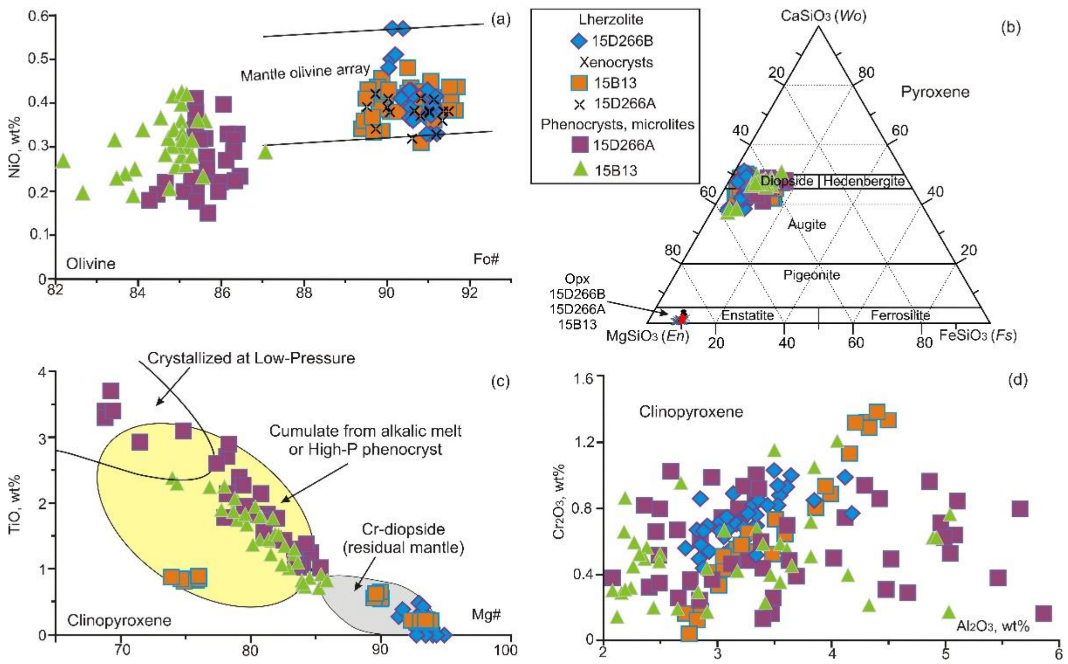

Figure 11. Major-element compositions of olivine and pyroxene in Alba Guyot volcanic and mantle rocks. Mantle olivine arrays in (a) are quoted from Takahashi et al. [25]. (c) TiO_2 vs. Mg# clinopyroxene classification from Wass [26].

Most of analyses for *clinopyroxene* from basanite and tuff fall within the diopside field in the *Wo–Fs–En* diagram (Figure 11b; Tables 2–4). Most highly magnesian diopside-augite (Mg#, 100·Mg/(Mg+Fe) 91.4–94.8) containing 0.4–1 wt% Cr_2O_3 and the smallest amount of TiO_2 (< 0.35 wt%) is found in lherzolite and in peridotite xenoliths from tuff (Figure 11c,d). Cpx xenocrysts in tuff have a larger Mg# range than those from lherzolite: 89.7–93.9 to 73.9–76. Cpx phenocrysts and microlites from basanite and tuff show negative correlation between Mg# (69–86) and TiO_2 contents (0.9–3.7 wt%), while Cr_2O_3 varies up to 1 wt% (Figure 11b,c).

Orthopyroxene (89–91 mol% En, enstatite) occurs in lherzolite as a rock-forming phase or as Cpx-hosted exsolution lamelli, as well as in Cpx xenocrysts from tuff and basanite (Figure 10c,f,l). Opx from lherzolite also encloses thin diopside lamelli. Opx xenocrysts from basanite and tuff are partly or fully replaced by the Cpx + Ol aggregate (Figure 10c,l). Opx in all rock samples has rather uniform major-oxide chemistry, with 54–56 wt% SiO_2, 32–34 wt% MgO, 6–7 wt% FeO, 2–4 wt% Al_2O_3, 0.4–0.8 wt% Cr_2O_3, and 0.3–0.7 wt% CaO (Tables 3 and 4; Figure 11b). Opx in a small peridotite xenolith from tuff encloses *phlogopite* containing 38.4 wt% SiO_2, 0.9 wt% TiO_2, 14.1 wt% Al_2O_3, 1 wt% Cr_2O_3, 23.5 wt% MgO, 1.2 wt% Na_2O, 8.4 wt% K_2O, 0.7 wt% BaO, 0.2 wt% NiO, and 0.1 wt% Cl. Clinopyroxene from lherzolite likewise hosts sporadic phlogopite inclusions.

Spinel-group minerals in lherzolite and peridotite xenoliths from tuff have highest Al_2O_3 contents (36–54 wt%) and Mg#, Mg/(Mg+Fe^{2+}) 0.70–0.85, at low Cr#, Cr/(Cr+Al) 0.13–0.38 and TiO_2 < 0.38 wt% (Tables 2–4, Figure 12). Spinel from basanite and some peridotite xenoliths in tuff show lower Mg# of 0.6–0.7 and higher Cr# (0.29–0.73), while Sp in tuff has the lowest Mg# (0.33–0.48) and highest Cr# 0.68–0.73 values (Figure 12b). The Mg# values in Sp from all analyzed rocks are in negative correlation with Cr# and total iron (Fe^{2+} + Fe^{3+}). TiO_2 in Sp from basanite and tuff varies from 0.2 to 4.8 wt% (2–4 wt% on average) (Figure 12c).

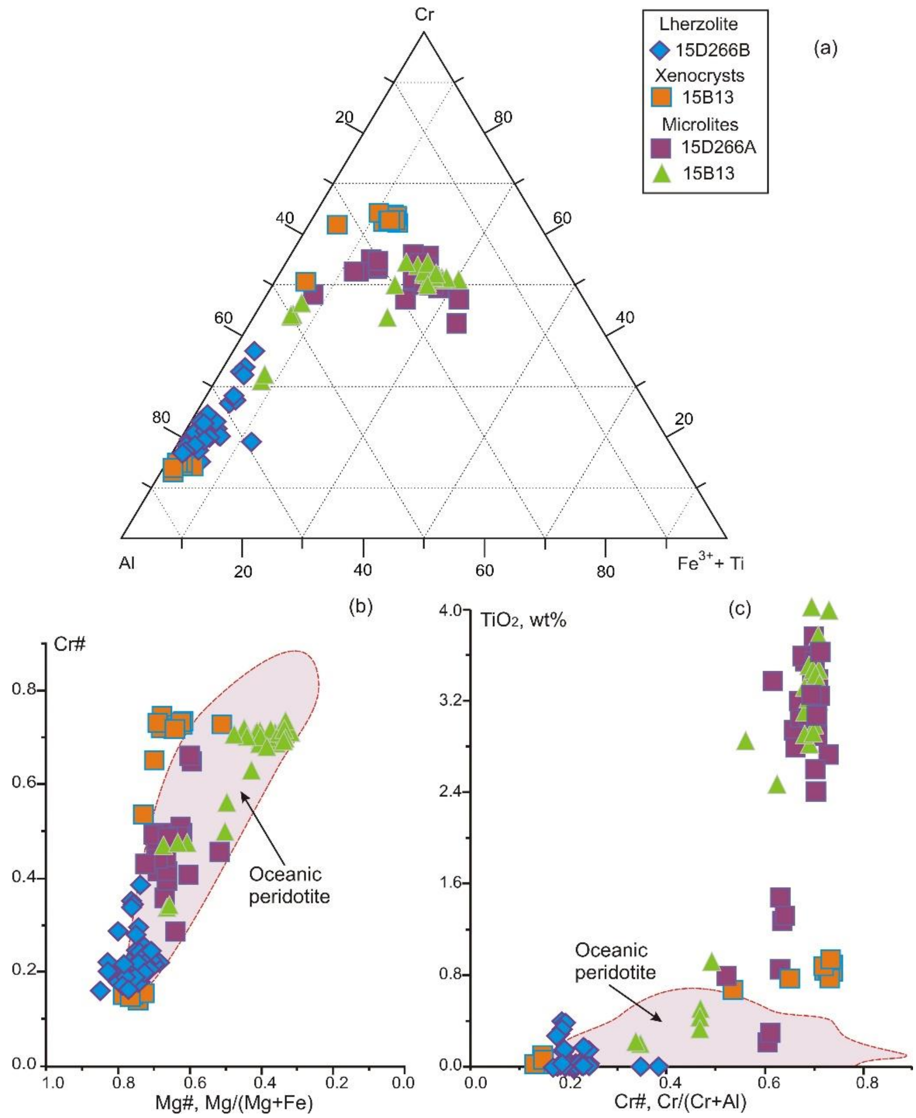

Figure 12. Major-element compositions of spinel-group minerals in Alba Guyot volcanic and mantle rocks. Dashed lines in panels (c,d) contour the fields of oceanic spinel from Mariana Trough, Mariana Trench, Parece Vela Basin, and Yap Trench, after Chen et al. [27].

Alkaline *silicate glass* (25–30 wt% according to mass-balance calculations) fills interstices between phenocrysts and microlites in the basanite matrix (Table 2, Figure 10a-c). Its composition normalized to 100 wt% plots within the field of Tephri-Phonolite and Phonolite in the TAS diagram for volcanic rocks (Figure 13). The glass contains more Na_2O than K_2O (5.4–8.7 wt% against 4.6–6.1 wt%) and minor amounts of FeO (3.3–6.8 wt%), CaO (1.6–4.6 wt%), MgO (0.4–1.2 wt%), TiO_2 (1–2.2 wt%), MnO (≤ 0.2 wt%), BaO (0.3–0.7 wt%), P_2O_5 (0.7–2.2 wt%), SO_3 (≤ 1 wt%), and Cl (0.3–0.5 wt%). Raman spectroscopy revealed molecular H_2O which may reach 4–6 wt%, as inferred from deficit of totals in SEM-EDS analyses.

The amounts of glass and palagonite are greater in volcanic clasts from tuff than in basanite (Figure 10a,b,g,l). All glass in small clasts has been replaced by palagonite while glass particles in large clasts have reaction palagonite rims but their cores lack alteration signatures detectable by SEM EDS (Figure 10h). Compared to that from basanite, glass from tuff contains more CaO (6.8–10.8 wt%) and less $Na_2O + K_2O$ (3–4.9 wt% Na_2O, 2.9–4.2 wt% K_2O) (Table 4). Other major oxides in glass are 8.7–11.1 wt% FeO, 3.4–5.1 wt% MgO, 2.6–3.4 wt% TiO_2, 1–1.4 wt% P_2O_5, up to 0.3 wt% MnO, up to 0.5 wt% BaO, up to 0.4 wt% SO_3, 0.1–0.2 wt% Cl, and 3–5 wt% H_2O (according to Raman spectroscopy and SEM EDS). In the TAS diagram, glass plots in the fields of Tephrite-Basanite and Phono-Tephrite (Figure 13).

 doi:10.20944/preprints202408.1315.v1

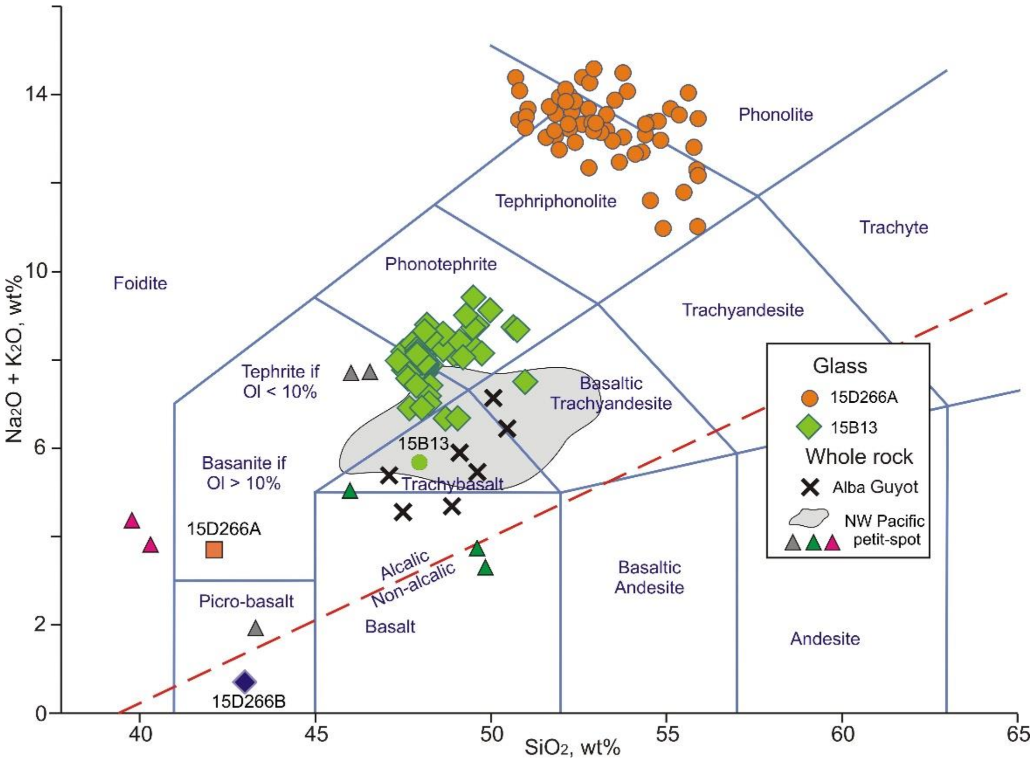

Figure 13. Total alkali vs. silica (TAS) diagram for volcanic rocks, after Le Bas et al. [28] and Irvine, Baragar [29]. The compositions of the whole rock petit-spot basaltic rocks are represented for Alba Guyot from Peretyazhko et al. [9], NW Pacific and unusual compositions by triangles from Hirano, Machida [30] and Mikuni et al. [31]. The data are plotted as the total 100 wt%.

3.3. $^{40}Ar/^{39}Ar$ Age of Basanite

Incremental heating $^{40}Ar/^{39}Ar$ dating of volcanic rocks weathered by sea water was applied to acid-leached groundmass samples. The results include plateau ages and $^{39}Ar/^{40}Ar - ^{36}Ar/^{40}Ar$ isochron ages, mainly for fractions of K-bearing minerals, such as amphibole or plagioclase [6,32]. Isotope measurements were performed for two specimens of sample 15D266A (Table 5). One specimen (197.51 mg) yielded a 19.9 ± 0.8 Ma $^{40}Ar/^{39}Ar$ age calculated using 100% of cumulative ^{39}Ar released (Figure 14). However, no statistically justified plateau age could be obtained for the other specimen (246.34 mg), because of large variance and error at 675, 975, 1025, 1075, and 1150 °C temperature steps. The calculated age values were 18.3 ± 0.4 Ma (Miocene) at the 500–600 °C (53.2% cumulative ^{39}Ar released) and from 16.1 ± 1.9 Ma to 24.0 ± 0.9 Ma at 750–925 °C (24.6% cumulative ^{39}Ar) steps (Figure 14; Table 5). The analytical problems with the second specimen may be due to rock alteration by sea water and to the presence of amorphous glass preserved partly in large specimen (246.34 mg) of crushed and acid-leached basanite, as ^{39}Ar may move from one phase to another in a process known as recoil.

 doi:10.20944/preprints202408.1315.v1

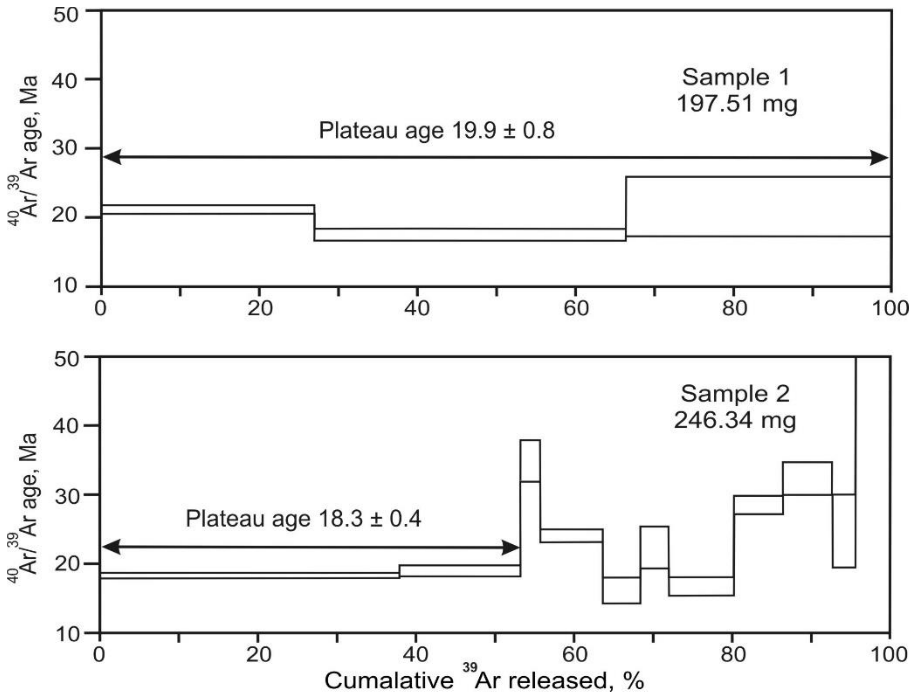

Figure 14. $^{40}Ar/^{39}Ar$ dating of basanite sample 15D266A.

Table 5. $^{40}Ar/^{39}Ar$ dating of basanite sample 15D266A.

T°C	^{40}Ar 10^{-9} cm^3 STP	$^{40}Ar/^{39}Ar$	$^{38}Ar/^{39}Ar$	$^{37}Ar/^{39}Ar$	$^{36}Ar/^{39}Ar$	Ca/K	$\sum^{39}Ar$ (%)	$^{40}Ar/^{39}Ar$ age, Ma
				197.51 mg; J=0.005355±0.000075				
850	24.5	3.0±0.002	0.018±0.00016	1.2345±0.0052	0.0028±0.00020	4.44	27.03	21.2±0.6
1000	24.6	2.1±0.002	0.017±0.00013	2.8868±0.0027	0.0009±0.00028	10.39	66.35	17.5±0.8
1150	17.6	1.7±0.003	0.021±0.00014	18.1577±0.0208	0.00017±0.00154	65.37	100.00	21.6±4.3
				246.34 mg; J=0.004992±0.000065				
500	85.4	3.2±0.002	0.018±0.00007	0.36±0.02	0.0038±0.00012	1.31	37.9	18.2±0.4
600	33.8	3.1±0.002	0.020±0.00010	0.51±0.03	0.0033±0.00030	1.83	53.2	18.9±0.8
675	9.2	5.2±0.009	0.027±0.00057	0.80±0.14	0.0043±0.00114	2.89	55.7	34.9±3.0
750	30.8	5.4±0.003	0.020±0.00016	1.36±0.03	0.0093±0.00032	4.90	63.7	24.0±0.9
800	21.1	6.2±0.006	0.022±0.00051	1.81±0.11	0.0150±0.00070	6.51	68.4	16.1±1.9
850	15.5	6.0±0.009	0.018±0.00080	1.64±0.12	0.0120±0.00116	5.91	72.0	22.3±3.1
925	29.8	5.0±0.004	0.020±0.00020	3.05±0.06	0.0108±0.00052	10.99	80.3	16.6±1.4
975	23.5	5.3±0.004	0.018±0.00043	3.29±0.07	0.0073±0.00050	11.84	86.4	28.5±1.4
1025	19.1	4.3±0.005	0.018±0.00047	8.07±0.09	0.0021±0.00088	29.06	92.7	32.3±2.3
1075	14.0	6.6±0.012	0.036±0.00046	22.48±0.16	0.0130±0.00202	80.94	95.6	24.7±5.3
1150	44.5	14.3±0.070	0.035±0.00086	78.75±0.40	0.0133±0.00668	283.50	100.0	90.7±17.0

Measurement errors are quoted at the ± 1σ level.

4. Discussion

4.1. Formation Conditions of Mineral Assemblages

The lack of plagioclase in basanite (sample 15D266A) and tuff (sample 15B13), as well as the presence of 3–6 wt% H_2O in volcanic glass, bear evidence of originally hydrous compositions of alkali-basaltic (basanitic) parent melts. Judging by the amount and chemistry of glass (Tables 2 and 4; Figure 13) and petrography of rocks (Figure 10 a-c,g-l), the sampled tuff formed during fragmentation of alkali-basaltic magma with a higher melt fraction than in the in the more crystalline erupted basanitic magma.

The analyzed samples enclose various mantle-derived fragments: a lherzolite xenolith in sample 15B266B and small peridotite xenoliths, as well as Cpx xenocrysts with Sp exsolution lamelli and Opx xenocrysts partially replaced by an Cpx + Ol aggregate in 15B13 tuff.

Lherzolite has a typically peridotitic protogranular texture (Figure 10d,e,f). Its crystallization *P-T* conditions were estimated previously using mineral chemistry data [9]. The crystallization temperature reconstructed by two-pyroxene (Cpx + Opx) geothermometry is 818 °C [33]. Other estimates we obtained with mineral thermobarometry for pressures in the 1.5–2 GPa interval: 719–732 °C from Cpx + Opx [34,35]; 754–767 °C from Fe-Mg–Ol/Sp [36], and 832–860 °C according to Ca–in–Opx thermobarometry [34]. The pressure calculated for the fixed temperature range between minimum and maximum estimates (720–860 °C) varies from 1.59 to 2.04 GPa or from 1.89 to 2.33 GPa, based on Cpx [37] and Cr–in–Cpx [38]geobarometers, respectively.

Thus, given the large uncertainty of the estimates, the equilibrium Ol + Cpx + Opx + Sp mineral assemblage of lherzolite presumably crystallized at 800 ± 50 °C and 2.0 ± 0.3 GPa, at depths 60 ± 5 km in oceanic lithosphere. Judging by the mineral chemistry of Sp, the melt fraction at crystallization of lherzolite mineral assemblage found using the empirical formula F,% = 10Ln(Cr#) + 24 [39] was within 6–10%. Furthermore, sporadic inclusions of phlogopite in the lherzolite xenolith and an Opx xenocryst from tuff provide implicit evidence for metasomatic changes in peridotite.

4.2. Evolution of Volcanism in Alba Guyot

The oldest volcanic edifices of Alba Guyot formed around 160 Ma within the Jurassic Magnetic Quiet Zone (JQZ) of the Pacific Plate [40], which was then located north of the Ontong Java Nui plateau in the Southern Hemisphere [41]. Large-scale Cretaceous volcanism in that part of the Pacific produced a Super-LIP [42], with numerous volcanoes in spreading zones along the Izanagi, Farallon, and Phoenix Plate boundaries.

The Alba Guyot slopes at 2400–3100 m sea depths are composed of amphibole-bearing basanite with an $^{40}Ar/^{39}Ar$ age of 102–100 Ma [5,6], while a part of the summit platform at a depth of 2200 m and the deeper (3400 m) Oma Vlinder satellite edifice consist of younger (95–93 Ma) basalts and hawaiites. Our $^{40}Ar/^{39}Ar$ determinations bracket the age of 1400 m thick (3600 to 2200 m deep) basalts, trachybasalts, and basaltic andesites in the upper portion of the Alba Guyot and Oma Vlinder satellite section between 112 and 86 Ma. In this respect, the Miocene age of basanite sample 15D266A from the vicinity of a small volcanic cone in the eastern margin of the guyot (Figure 1b) is unusual for the Cretaceous MST guyots and seamounts. The obtained $^{40}Ar/^{39}Ar$ age estimates have large variance though, in a range between 16.1 ± 1.9 Ma and 24.0 ± 0.9 Ma, the most probable values being 19.9 ± 0.8 Ma and 18.3 ± 0.4 Ma (Figure 14).

The bathymetric map of the guyot images five large and several small cones in the northwestern part (Figure 1b). Earlier sonar surveys and dredging at sites 15D21 and 15D18 revealed cones of basanite and tuff intercalated with organic (planktonic) limestone [3]. The cones were timed as Miocene proceeding from a single K/Ar date (15 ± 2 Ma) for dredged basanite sample 15D21, as well as from the biostratigraphy of calcareous nannofossils found in the carbonate cement of tuff. The chains of volcanic cones are aligned with large NW and NE faults which delineate topographically expressed scarps and a graben in the northern slope of the guyot [2]. Basanitic magma apparently ascended through deformed oceanic lithosphere in faults and at their junctions and erupted to build cones reaching 750 m high and 2.2 to 5.1 km diameter at base, upon the flat summit platform of the main guyot edifice.

Borehole 15B13 drilled near the small cone and dredging site 15D266 stripped a tuff layer (Figure 1b) deposited during eruption of basanitic magma, judging by the mineralogy of clasts (Figure 11,12). Furthermore, core samples from borehole 15B17 show a Miocene gap in the formation of the Fe-Mn crust (Figure 3). The presence of volcaniclastic rocks (tuff and tuffite), in the absence of hyaloclastic material on the guyot top, indicates that basanitic magma erupted above the sea level in the Miocene, between ~24 and 15 Ma (ages of basanite samples 15D266A and 15D21). The tuff cored at 15B13 was deposited in subaerial conditions while the deposition of tuffite from 15B17 occurred in shallow-water near-shore conditions.

Preprints.org (www.preprints.org) | NOT PEER-REVIEWED | Posted: 19 August 2024 doi:10.20944/preprints202408.1315.v1

According to previous estimates [2], the summit of the largest 750 m high basanitic cone near dredging site 15D21 is located at a sea depth of 551 m which is the shallowest over the summits of all subsea MST edifices. Therefore, it was the last submerged mountain in the MST. As evidenced by biostratigraphic data for 15B13 core (Figure 2), carbonate sediments containing calcareous nannofossils of biozones CN7 and CN8 were deposited on porous tuff surfaces in the Middle-Late Miocene, about 10 to 7 Ma, when the guyot was already below the sea level. Most likely, calcareous nannoplakton from biozone CN9 appeared in the 15B17 tuffite layer around 6 Ma, in the Late Miocene (Figure 3). The evolution of the edifice was completed by the latest event of Fe-Mn crust precipitation (*Unit III*) in the Pleistocene, after 1.8 Ma. The age of the crust covering samples of basanite 15D266A, lherzolite xenolith 15D266B, and surfaces of cores 15B13 and 15B17 (Figure 2,3,10d) is constrained by the presence of calcareous nannofossils that belong to biozones CN19 and CN20.

4.2. Petit-Spot Volcanoes in the Pacific Plate and in Alba Guyot

There are several known occurrences of Cenozoic petit-spot volcanism associated with an unusual geodynamic setting of the Pacific Plate [43,44]. Petit-spot volcanoes younger than 8.5 Ma were found not far from the Japan trench, along the subducting slab front [43], and even younger (< 3 Ma) small cones were discovered recently on the abyssal plain near Marcus (Minamitorishima) Island, about 2000 km east of the Mariana trench [44]. Geodynamic models [45–48] attribute petit-spot volcanic activity to stress release into trenches during the Pacific subduction and related faulting. The flexure of the > 100 km thick Pacific Plate in the Cenozoic subduction zone produced tension in the oceanic lithosphere, which led to faulting from the Lithosphere–Asthenosphere Boundary (LAB) or Low-Velocity Zone (LVZ) level and to the related petit-spot alkali basaltic volcanism. Therefore, alkali-basaltic melts may result from decompression (adiabatic) melting of the asthenospheric and metasomatized oceanic lithospheric material under the effect of tectonic motions, without any plume involved [8–10,44,45,47–49].

The rejuvenated Cenozoic petit-spot volcanism apparently produced the Miocene basanitic cones and tuff layers on the summit platform of Alba Guyot (Figure 1b). This inference is consistent with the location of MST guyots near the Mariana trench in the northwestern segment of the Pacific Plate and with the alkali-basaltic signatures of the Alba basanite. The compositions of glass from tuff (15B13) and basanite (15D266A) plot the most alkaline trend in the TAS diagram (Figure 13), and our data have provided the first evidence of basanite in the Cenozoic volcanics of the Pacific Plate. Basanite sample 15D266A after Peretyazhko et al. [9] shares geochemical similarity (incl. Sr, Nd, and Pb isotopic ratios) with petit-spot basalts, trachybasalts, and basaltic trachyandesites reported previously from the Pacific and Indian Oceans [30,31,50–52]. Namely, similar shapes are observed in multi-element patterns normalized to primitive mantle, with typical Zr–Hf and Ti depletion, and in chondrite-normalized REE + Y spectra with $(La/Yb)_N$ up to 31 [9]. Petit-spot volcanics with such signatures presumably originate from alkali-basaltic melts produced by decompression partial melting of carbonatized peridotite in metasomatized oceanic lithosphere at the LAB or LVZ level [9,31,53].

Note also that the Miocene basanite volcanic cones found on Alba Guyot (Figure 1b) were described in the Russian literature more than twenty years ago [3], i.e., before the Japanese researchers [43] discovered Cenozoic petit-spot volcanoes in the Pacific Plate.

5. Conclusions

The previously published [9] and our new data on mineralogy, Miocene age of basanite, and biostratigraphy of core samples from Alba Guyot shed light on the history of its volcanism.

The Cretaceous volcanics in the upper part of the main guyot edifice and its satellite Oma Vlinder, between the 3600–2200 m bathymetric levels, were formed between 112 and 86 Ma. For the following ~60 myr, the guyot edifice became partially submerged, exposed to sea water weathering, and acquired a flat summit platform while the respective part of the Pacific Plate was moving to the Northern Hemisphere.

According to biostratigraphic evidence, a Fe-Mn crust (*units I-1* and *1-2b*) had formed no later than in the Oligocene (> 38 Ma) at the bathymetric level of borehole 15B17 and was then overlain by a layer of tuffite about ~6 Ma, in the Late Miocene (Figure 3).

Volcanic activity in the northeastern part of the guyot resumed in the Miocene (24–15 Ma) as voluminous outpourings of basanitic magma from several edifices which produced layers of tuff and tuffite above and below the sea level, respectively. The volcanic events inhibited the growth of Fe-Mn crusts around the summit of the guyot.

The mantle sources of basanitic magma were located at depths > 60 ± 5 km (according to *P-T* conditions inferred for the crystallization of the mineral assemblage in lherzolite), in metasomatized (carbonatized) oceanic lithosphere, possibly, at the LAB level. The basanitic magma ascended along deep faults in the oceanic lithosphere and Cretaceous Alba Guyot main edifice and entrapped fragments of mantle rocks (lherzolite xenoliths and Ol, Cpx, and Opx xenocrysts).

In Middle-Late Miocene (10–6 Ma), after the Alba Guyot had submerged, carbonates containing calcareous nannofossils were deposited on porous surfaces of tuff (15B13) and during the formation of a tuffite layer (15I17). Precipitation of the Fe-Mn crust (*Unit III*) recommenced during the Pliocene-Pleistocene (< 1.8 Ma) when the guyot summit reached favorable sea depths.

The numerous small and large volcanic cones found on the Alba summit platform (Figure 1b) provide the first evidence of voluminous Miocene petit-spot basanitic volcanism upon the Cretaceous guyots and seamounts of the Pacific.

Author Contributions: Conceptualization and investigation, I.S.P.; field sampling, I.A.P.; writing, review, and editing, all authors; Visualization, I.A.P. and E.A.S. All authors have read and agreed to the published version of the manuscript.

Funding: The study was carried out as part of Basic Research Program 0284-2021-0006 of the Russian Academy of Sciences.

Acknowledgments: We would like to thank crew members of R/V *Gelendzhik* (JSC *Yuzhmorgeologiya*) for sampling work and support during the cruises of 2019–2020. We are grateful to our colleagues: Yudin D.S. (Sobolev Institute of Geology and Mineralogy, Novosibirsk) for Ar-Ar dating, Cherbakov Yu.D. (Vinogradov Institute of Geochemistry, Irkutsk) and Khromova E.A. (Geological Institute, Ulan-Ude) for SEM-EDS measurements.

Conflicts of Interest: The authors declare no conflict of interest.

References

1. Volokhin, Yu.G.; Melnikov, M.E.; Shkolnik, E.L.; Vasiliev, B.I.; Govorin, I.N.; Khersberg, L.B.; Zadornov, M.V.; Baturin, G.N.; Mechetin, A.V.; Chudaev, O.V.; Michailik, E.V.; Konovalov, Y.I.; Evlanov, Y.B.; Malyarenko, A.N.; Tatarin, I.A.; Govorov, G.I.; Simanenko, V.P.; Martinov, Y.A.; Panchenko, I.V.; Dmitriev, Y.D.; Golubeva, E.D.; S'edin, V.T.; Birulina, M.G.; Burikova, I.A.; Gerasimova, G.I.; Kiselev, V.V.; Pletnev, S.P.; Popova, T.V.; Oktyabrskiy, R.A.; Senkova, T.V. Guyots of the Western Pacific and their Mineralisation. Moscow, 1995, Nauka, 368 p. (in Russian).
2. Pletnev, S.P.; Melnikov, M.E.; S'edin, V.T.; Sedysheva, T.E.; Avdonin, V.V.; Anokhin, V.M.; Zakharov, Y.D.; Punina, T.A.; Smirnova, O.L. Geology of Guyots in the Magellan Seamounts (Pacific Ocean): Vladivostok, 2020, Dalnauka, 200 p. (in Russian).
3. Melnikov, M.Ye.; Podschuveit, V.B.; Pulyaeva, I.A.; Nevretdinov, E.B. Middle Miocene volcanic structures on the Dalmorgeologiya Guyot (Magellan Seamounts, Pacific Ocean). Russ. J. Pacific Geol., 2000, 19(5), 38–46.
4. Melnikov, M.Ye.; Pletnev, S.P.; Anokhin, V.M.; Sedysheva, T.E.; Ivanov, V.V. Volcanic edifice on guyots of the Magellan Seamounts (Pacific Ocean). Russ. J. Pacific Geol., 2016, 35(6), 46–53. https://doi.org/10.1134/S1819714016060038
5. Koppers, A.A.P.; Staudigel, H.; Wijbrans, J.R.; Pringle, M.S. The Magellan seamount trail: implications for Cretaceous hotspot volcanism and absolute Pacific Plate motion. Earth and Planetary Science Letters (EPSL), 1998, 163, 53–68. https://doi.org/10.1016/S0012-821X(98)00175-7
6. Koppers, A.A.P.; Staudigel, H.; Wijbrans, J.R. Dating crystalline groundmass separates of altered Cretaceous seamount basalts by the $^{40}Ar/^{39}Ar$ incremental heating technique. Chem. Geol., 2000, 166, 139–158. https://doi.org/10.1016/S0009-2541(99)00188-6

7. Wei, H.; Zhang, G-L.; Zhang, Ji.; Shi, X-F.; Castillo, P.R.; Zhang, Y.; Zhang, W-F.; Xu, Y-G.; Li, H-Y.; Hui Zhang, H. Overlapping hotspot tracks and melts from diffuse plume materials in the upper mantle generated intraplate seamount groups in the West Pacific. Earth and Planetary Science Letters (EPSL), 2024, V. 643. https://doi.org/10.1016/j.epsl.2024.118901
8. Peretyazhko, I.S.; Savina, E.A. Chemistry and crystallization conditions of minerals in metasomatized oceanic lithosphere and basaltic rocks of Govorov Guyot, Magellan Seamounts, Pacific Ocean. Minerals, 2022, 12(10):1305. https://doi.org/10.3390/min12101305
9. Peretyazhko, I.S.; Savina, E.A.; Pulyaeva, I.A.; Yudin, D.S. Intraplate volcanism of the Alba Guyot. Geodynamic formation models of the Magellan Seamounts in the Pacific Ocean for 100 million years: Russ. Geol. Geophys., 2023, 64 (1): 1–27. https://doi.org/10.2113/RGG20214422
10. Peretyazhko, I.S.; Savina, E.A. Cretaceous intraplate volcanism of Govorov Guyot and formation models of the Magellan seamounts, Pacific Ocean. International Geology Review, 2023, 65(16):2479-2505. https://doi.org/10.1080/00206814.2022.2145512
11. Pulyaeva, I.A. Stratification of ferromanganese crusts on the Magellan seamounts: In: Proceedings of 30th International Geological Congress, 8-14 August 1996 1997?, Beijing, Vol. 13, 111–128.
12. Glasby, G.P.; Ren, X.; Shi, X.; Pulyaeva, I.A. Co-rich Mn crusts from the Magellan seamounts cluster: the long journey through time. Geo-Mar Lett., 2007, 27:315–323.
13. Pulyaeva, I.A.; Hein, J.R. Hydrogenetic Fe-Mn crusts from the Atlantic and Pacific oceans: geological evolution and conditions of formation. Marine minerals: Recent Innovations in Technology. UMI, Hawaii, 2011, 11.
14. Lavrent'ev, Yu.G.; Karmanov, N.S.; Usova, L.V. Electron probe microanalysis of minerals: microprobe or scanning electron microscope? Russian Geology and Geophysics, 2015, 56(8), 1154–1161. https://doi.org/10.1016/j.rgg.2015.07.006
15. Peretyazhko, I.S. *CRYSTAL* – Applied software for mineralogists, petrologists, and geochemists. Zapiski Rossiiskogo Mineralogicheskogo Obshchestva, 1996, 3, 141–148 (in Russian).
16. Martini, E. Standard Neogene calcareous nannoplankton zonation. In: E. Martini, T. Worsley (ed.), Naturfa, 1970, 225, 289–290.
17. Martini, E. Standard Tertiary and Quaternary calcareous nannoplankton zonation. In: Farinacci A (ed.) Proceedings of 2nd Planktonic Conference, 1971, V. 2. Edizioni Tecnoscienza, Roma, 1225–1230.
18. Bukry, D. Coocolith stratigraphy, eastern equatorial Pacific, Leg. 16, Deep Sea Drilling Project. In: Initial Reports DSDP, 1973a, 16, 653–711.
19. Bukry, D. Biostratigraphy of Cenozoic marine sediment by calcareous nannofossils. Micropaleontology, 1978, 24(1), 44–60.
20. Bukry, D. Phytoplankton stratigraphy, Deep Sea Drilling Project, Leg 20, Western Pacific Ocean. In: Initial Reports DSDP, 1973b, 20, 307–317.
21. Bukry, D. Phytoplankton stratigraphy, Deep Sea Drilling Project, Leg 20, Western Pacific Ocean. In: Initial Reports DSDP, 1973b, 20, 307–317.
22. Okada, H; Bukry, D. Supplementary modification and introduction of code numbers to the low latitude coccolith biostratigraphic zonation. Marine Micropaleontology, 1980, 5:321–325.
23. Perch-Nielsen, K. Cenozoic calcareous nannofossils. In H.M. Bolli, J.B. Saunders and K. Perch-Nielsen (Eds.), Plankton Stratigraphy (Cambridge Earth Science Series) Cambridge University Press, 1985, 427–554.
24. Shumenko, S.I. Guide to Microfossils of the USSR. Leningrad, Nedra, 1987, 1, 198 p. (in Russian)
25. Takahashi, E.; Uto, K.; Schilling, J-G. Primary magma compositions and Mg/Fe ratios of their mantle residues along Mid Atlantic Ridge 29° N to 73°N. Technical report of ISEI Okayama University Series, 1987, A 9:1–4.
26. Wass, S.Y. Multiple origins of clinopyroxenes in alkali basaltic rocks. Lithos, 1979, 12:115–132. https:// doi. org/ 10. 1016/ 0024- 4937(79) 90043-4
27. Chen, L.; Tang, L.; Li, X.; Dong, Y.; Xing; Yu, X.; Ding, W. Geochemistry of peridotites from the Yap Trench, Western Pacific: Implications for subduction zone mantle evolution. Int. Geol. Rev. 2019, 61, 1037–1051. https://doi.org/10.1080/00206814.2018.1484305
28. Le Bas, M. J.; Le Maitre, R.; Strackeisen, A.; Zanettin, B. A chemical classification of volcanic rocks based on the total alkali–silica diagram. J. Petrol., 1986, 27, 745–750. https://doi.org/10.1093/petrology/27.3.745
29. Irvine, T.N.; Baragar, W.R.A. A Guide to the Chemical Classification of the Common Volcanic Rocks. Can. J. Earth Sci., 1971, 8, 523–548. https://doi.org/10.1139/e71-055

30. Hirano, N.; Machida, S. The mantle structure below petit-spot volcanoes, Commun. Earth Environ., 2022, 3, 110. https://doi.org/10.1038/s43247-022-00438-1
31. Mikuni, K.; Hirano, N.; Machida, S.; Sumino, H.; Akizawa, N.; Tamura, A.; Morishita, T.; Kato, Y. Contribution of carbonatite and recycled oceanic crust to petit-spot lavas on the western Pacific Plate. Solid Earth, 2024, 15, 167–196. https://doi.org/10.5194/se-15-167-2024
32. Heaton, D.E.; Koppers, A.A.P. High-resolution $^{40}Ar/^{39}Ar$ geochronology of the Louisville seamounts IODP expedition 330 drill sites: Implications for the duration of hot spot-related volcanism and age progressions. Geochemistry, Geophysics, Geosystems (GGG), 2019, 20, 4073–4102. https://doi.org/10.1029/2018GC007759.
33. Wells, P.R.A. Pyroxene thermometry in simple and complex systems. Contrib. Mineral. Petrol., 1977, 46, 129–139. http://doi.org/10.1007/BF00372872
34. Brey, G.P.; Köhler, T. 1990. Geothermobarometry in four-phase lherzolites II: New thermobarometers and practical assessment of existing thermobarometers. J. Petrol., 1990, 31 (6), 1353–1378, http://doi.org/ 10.1093/petrology/31.6.1353
35. Taylor, W. An experimental test of some geothermometer and geobarometer formulations for upper mantle peridotites with application to the thermobarometry of fertile lherzolite and garnet websterite. Neues Jahrbuch Mineral. Abhandlungen, 1998, 172:381–408. http://doi.org/10.1127/njma/172/1998/381
36. O'Neill, H.St.C.; Wall, V.J. The olivine-orthopyroxene-spinel oxygen-geobarometer, the nickel precipitation curve and the oxygen fugacity of the earth's upper mantle. J. Petrol., 1987, 28, 1169–1191. http://doi.org/10.1093/petrology/28.6.1169
37. Nimis, P.; Taylor, W.R. Single clinopyroxene thermobarometry for garnet peridotites. Part I. Calibration and testing of a Cr-in-Cpx barometer and an enstatite-in-Cpx thermometer. Contrib. Mineral. Petrol., 2000, 139(5), 541–554. https://doi.org/10.1007/s004100000156
38. Sudholz, Z.J.; Yaxley, G.M.; Jaques, A.L.; Brey, G.P. Experimental recalibration of the Cr-in-clinopyroxene geobarometer: improved precision and reliability above 4.5 GPa. Contrib. Mineral. Petrol., 2021, 176:11. http://doi.org/10.1007/s00410-020-01768-z
39. Hellebrand, E.; Snow, J.E.; Dick, H.J.B.; Hofmann, A.W. Coupled major and trace elements as indicators of the extent of melting in mid-ocean-ridge peridotites. Nature, 2001, 410(6829), 677–681. https://doi.org/10.1038/35070546
40. Tivey, M.A.; Sager, W.W.; Lee, S.M.; Tominaga, M. Origin of the Pacific Jurassic quiet zone. Geology, 2006, 34, 789–792. https://doi.org/10.1130/G22894.1
41. Hochmuth, K.; Golf, K.; Uenzelmann-Neben, G. Playing jigsaw with Large Igneous Provinces – A plate tectonic reconstruction of Ontong Java Nui, West Pacific. Geochemistry, Geophysics, Geosystems (GGG), 2015, 16, 3789-3807. http://doi.org/10.1002/2015GC006036
42. Seton, M.; Müller, R.D.; Zahirovic, S.; Gain, C.; Torsvik, T.; Shephard, G.; Talsma, A.; Gurnis, M.; Turner, M.; Maush, S.; Chandler, M. Global continental and ocean basin reconstructions since 200Ma. Earth Science Review, 2012, 113(3-4), 212–270. http://doi:10.1016/j.earscirev.2012.03.002
43. Hirano, N.; Kawamura, K.; Hattori, M.; Saito, K.; Ogawa, Y. A new type of intra-plate volcanism; Young alkali-basalts discovered from the subducting Pacific Plate, Northern Japan Trench. Geophys. Res. Let., 2001, 28, 2719–2722. http://doi.org/ 10.1029/2000GL012426
44. Hirano, N.; Machida, S.; Sumino, H.; Shimizu, K.; Tamura, A.; Morishita, T.; Iwano, H.; Sakata, S.; Ishii, T.; Arai, S.; Yoneda, S.; Danhara, T.; Hirata, T. Petit-spot volcanoes on the oldest portion of the Pacific Plate. Deep-Sea Research Part I, 2019, 154, 103142. http://doi.org/10.1016/j.dsr.2019.103142
45. Hirano, N. Petit-spot volcanism: a new type of volcanic zone discovered near a trench, Geochem. J., 45, 157–167. https://doi.org/10.2343/geochemj.1.0111, 2011.
46. Harigane, Y.; Mizukami, T.; Morishita, T.; Michibayashi, K.; Abe, N.; Hirano, N. Direct evidence for upper mantle structure in the NW Pacific Plate: Microstructural analysis of a petit-spot peridotite xenolith: Earth and Planetary Science Letters (EPSL), 2011, 302, 194–202. http://doi.org/10.1016/j.epsl.2010.12.011
47. Machida, S.; Kogiso, T.; Hirano, N. Petit-spot as definitive evidence for partial melting in the asthenosphere caused by CO_2. Nature Communications, 2017, 8, 14302. http://doi. org/10.1038/ncomms14302
48. Pilet,S.; Baker, M.B.; Stolper, E.M. Metasomatized lithosphere and the origin of alkaline lavas. Science, 2008, 320, 916–919. http://doi.org/10.1126/science.1156563

 doi:10.20944/preprints202408.1315.v1

49. Pilet, S.; Abe, N.; Rochat, L.; Kaczmarek, M.A.; Hirano, N.; Machida, S.; Buchs D.M.; Baumgartner, P.O.; Müntener, O. Pre-subduction metasomatic enrichment of the oceanic lithosphere induced by plate flexure. Nature Geosciences, 2016, 9, 898–903. http://doi.org/10.1038/ngeo2825
50. Taneja, R.; Rushmer, T.; Blichert-Toft, J.; Turner, S.; O'Neill, C. Mantle heterogeneities beneath the Northeast Indian Ocean as sampled by intra-plate volcanism at Christmas Island. Lithos, 2016, 262, 561–575, https://doi.org/10.1016/j.lithos.2016.07.027
51. Reinhard, A.A.; Jackson, M.G.; Blusztajn, J.; Koppers, A.A.P.; Simms, A.R.; Konter, J.G. "Petit Spot" rejuvenated volcanism superimposed on plume-derived Samoan Shield volcanoes: Evidence from a 645m drill core from Tutuila Island, American Samoa. Geochemistry, Geophysics, Geosystems (GGG), 2019, 20, 1485–1507. https://doi.org/10.1029/2018GC007985
52. Falloon, T.J.; Hoernle, K.; Schaefer, B.F.; Bindeman, I.N.; Hart, S.R.; Garbe-Schonberg, D.; Duncan, R.A. Petrogenesis of lava from Christmas Island, Northeast Indian Ocean. Implications for the nature of recycled components in non-plume intraplate settings. Geosciences, 2022, 12, 118, https://doi.org/10.3390/geosciences12030118
53. Dasgupta, R.; Hirschmann; M.M.; McDonough, W.F.; Spiegelman, M.; Withers, A.C. Trace element partitioning between garnet lherzolite and carbonatite at 6.6 and 8.6 GPa with applications to the geochemistry of the mantle and of mantle-derived melts. Chem. Geol., 2009, 262, 57–77. http://doi.org/10.1016/j. chemgeo.2009.02.004